

# H I, star formation and tidal dwarf candidate in the Arp 305 system

Chandreyee Sengupta,<sup>1,2</sup>★ T. C. Scott,<sup>3,4</sup> S. Paudel,<sup>1,2</sup> K. S. Dwarakanath,<sup>5</sup>  
D. J. Saikia<sup>6,7</sup> and B. W. Sohn<sup>2</sup>

<sup>1</sup>Department of Astronomy, Yonsei University, 50 Yonsei-ro, Seodaemun-gu, Seoul 03722, Republic of Korea

<sup>2</sup>Korea Astronomy and Space Science Institute, 776, Daedeokdae-ro, Yuseong-gu, Daejeon 305-348, Republic of Korea

<sup>3</sup>Institute of Astrophysics and Space Sciences (IA), Rua das Estrelas, P-4150-762 Porto, Portugal

<sup>4</sup>Centre for Astrophysics Research, University of Hertfordshire, College Lane, Hatfield AL10 9AB, UK

<sup>5</sup>Raman Research Institute, Bangalore 560 080, India

<sup>6</sup>National Centre for Radio Astrophysics, Tata Institute of Fundamental Research, Pune 411 007, India

<sup>7</sup>Cotton University, Panbazar, Guwahati 781 001, India

Accepted 2017 April 7. Received 2017 April 6; in original form 2016 October 14

## ABSTRACT

We present results from our Giant Metrewave Radio Telescope (GMRT) H I observations of the Arp 305 system. The system consists of two interacting spiral galaxies NGC 4016 and NGC 4017, a large amount of resultant tidal debris and a prominent tidal dwarf galaxy (TDG) candidate projected within the tidal bridge between the two principal galaxies. Our higher resolution GMRT H I mapping, compared to previous observations, allowed detailed study of smaller scale features. Our H I analysis supports the conclusion in Hancock et al. that the most recent encounter between the pair occurred  $\sim 4 \times 10^8$  yr ago. The GMRT observations also show H I features near NGC 4017 that may be remnants of an earlier encounter between the two galaxies. The H I properties of the bridge TDG candidate include  $M_{\text{H I}} \sim 6.6 \times 10^8 M_{\odot}$  and  $V_{\text{H I}} = 3500 \pm 7 \text{ km s}^{-1}$ , which are in good agreement with the velocities of the parent galaxies. Additionally, the TDG's H I linewidth of  $30 \text{ km s}^{-1}$  and modest velocity gradient together with its star formation rate of  $0.2 M_{\odot} \text{ yr}^{-1}$  add to the evidence favouring the bridge candidate being a genuine TDG. The bridge TDG's *Spitzer* 3.6 and  $4.5 \mu\text{m}$  counterparts with a [3.6]–[4.5] colour  $\sim -0.2$  mag suggests that stellar debris may have seeded its formation. Future spectroscopic observations could confirm this formation scenario and provide the metallicity, which is a key criterion for the validation of TDG candidates.

**Key words:** galaxies: dwarf – galaxies: individual: Arp 305 – galaxies: interactions – galaxies: spiral – galaxies: star formation.

## 1 INTRODUCTION

Interactions between gas-rich galaxy pairs can result in massive H I stripping from the parent galaxies' H I discs (e.g. Duc et al. 1997, 2000; Smith et al. 2007, 2010; Sengupta et al. 2015). Much of this stripped H I may fall back into the gravitational potential of either of the pair or, at later stages, the new merged galaxy or be incorporated into the intragroup medium. Under the right conditions, new star formation (SF) may arise within the evolving H I debris (Hibbard et al. 2005; Neff et al. 2005; Smith et al. 2010; de Mello et al. 2012; Torres-Flores et al. 2012). If the cold gas (H I and molecular gas) densities are sufficient and environmental conditions are favourable, the evolution of the cold gas and stellar debris may include the formation of self-gravitating bodies with masses typical of dwarf galaxies, known as tidal dwarf galaxies (TDGs; Duc & Mirabel 1999; Duc et al. 2000; Smith et al. 2007, 2010). H  $\alpha$  and

ultraviolet (UV) emission trace SF on time-scales of  $10^7$  and  $10^8$  yr, respectively (Boselli et al. 2009). So, if a TDG has an H I counterpart and it has stellar populations formed later than the time when its parent galaxies began interacting, this can provide evidence for *in situ* SF. Cases where a TDG forms from pure gas collapse, as opposed to gas collapse promoted by the gravitational potential of stellar debris from the parents, can be considered as a separate class of TDGs (Duc, Bournaud & Masset 2004). Interacting pairs thus provide a unique laboratory to study the impact of interactions on the gaseous and the stellar components of the parent galaxies as well as the conditions under which neutral gas debris collapses to form star clusters and TDGs.

Arp 305 is an interacting pair of galaxies (NGC 4016 and NGC 4017) with an  $M_*$  ratio of  $\sim 1:3$  and heliocentric optical radial velocities<sup>1</sup> of  $3441 \pm 1$  and  $3449 \pm 2 \text{ km s}^{-1}$ , respectively. Further basic properties of the pair are set out in Table 1. NGC 4016 and

\* E-mail: sengupta.chandreyee@gmail.com

<sup>1</sup> From Hyperleđa (Makarov et al. 2014).

**Table 1.** Properties of the Arp 305 pair.

Property <sup>a</sup>	Units	NGC 4016	NGC 4017
$V_{\text{radial(optical)}}$	(km s <sup>-1</sup> )	3441 ± 1	3449 ± 2
RA	(h:m:s)	11:58:29.02	11:58:45.67
Dec.	(d:m:s)	+27:31:43.62	+27:27:08.79
Distance <sup>b</sup>	(Mpc)	50	50
D <sub>25</sub> major/minor	(arcmin)	1.5 × 0.8	1.8 × 1.4
D <sub>25</sub> major/minor	(kpc)	21.8 × 11.6	26.1 × 20.3
Inclination	(°)	59.8	48.2
Morphology		SBdm	SABbc
$B_T$	(B-band mag)	14.54 ± 0.13	14.34 ± 0.13
Stellar mass $M_*$	(10 <sup>10</sup> M <sub>⊙</sub> )	0.6	2.7.

<sup>a</sup>All data are from NED, except  $V_{\text{radial(optical)}}$  and inclination, which are from Hyperleda.

<sup>b</sup>See Section 1.

NGC 4017 are part of a small group of five galaxies (USGC U435) with its centre projected at 11:58:17.8 +27:47:03 with a radial velocity of 3456 km s<sup>-1</sup> (Ramella et al. 2002). The group velocity dispersion is 106 km s<sup>-1</sup>. The closest member of the group is projected ~22 arcmin (341 kpc) north of Arp 305. At optical and UV wavelengths, the Arp 305 pair displays clear signatures of a tidal interaction. These signatures include a figure of eight-shaped inner disc in NGC 4016, enhanced spiral arms in NGC 4017 and a tidal bridge remnant projected between the pair (Fig. 1) as well as four TDG candidates (Hancock et al. 2009).

A previous H I mapping of Arp 305 by van Moorsel (1983) with the Westerbork Synthesis Radio Telescope (WSRT) detected H I in both members of the pair and indicated that they are at an early stage of a wet merger. Hancock et al. (2009) used UV [*Galaxy*

*Evolution Explorer (GALEX)*] observations to identify 45 young star-forming (SF) clumps, including clumps within the four TDG candidates (see Fig. 1). The ‘bridge TDG’ candidate corresponds to the UV clumps 12, 13, 15 and 16 in fig. 2 of Hancock et al. (2009), with TDG1, TDG2 and TDG3 corresponding to UV clumps 11, 1 and 19, respectively, in the same figure.

In this paper, we present results from our Giant Metrewave Radio Telescope (GMRT) H I observations of the Arp 305 system. These observations have a higher spatial and velocity resolution than the previous WSRT H I observations (van Moorsel 1983), allowing the detailed study of small-scale H I morphology and kinematic features within the Arp 305 system, and, in particular, the SF regions. This paper also utilizes the Sloan Digital Sky Survey (SDSS), *Spitzer* and *GALEX* publicly available archive data and images. Section 2 sets out details of our observations, with observational results given in Section 3. We discuss the results in Section 4. A summary and concluding remarks are set out in Section 5. Using the average heliocentric velocity of the two principal galaxies from Hyperleda and assuming  $H_0$  to be 68 km s<sup>-1</sup> Mpc<sup>-1</sup> (Planck Collaboration I 2014), we adopt a distance of 50 Mpc for NGC 4016 and NGC 4017 and the TDGs. At this distance, the spatial scale is ~14.5 kpc arcmin<sup>-1</sup>. These values are comparable to those used by Hancock et al. (2009) and Smith et al. (2010). J2000 coordinates are used throughout this paper, including the figures.

## 2 OBSERVATIONS

H I observations of Arp 305 were carried out with the GMRT on 2014 July 12. A baseband bandwidth of 16 MHz was used for the

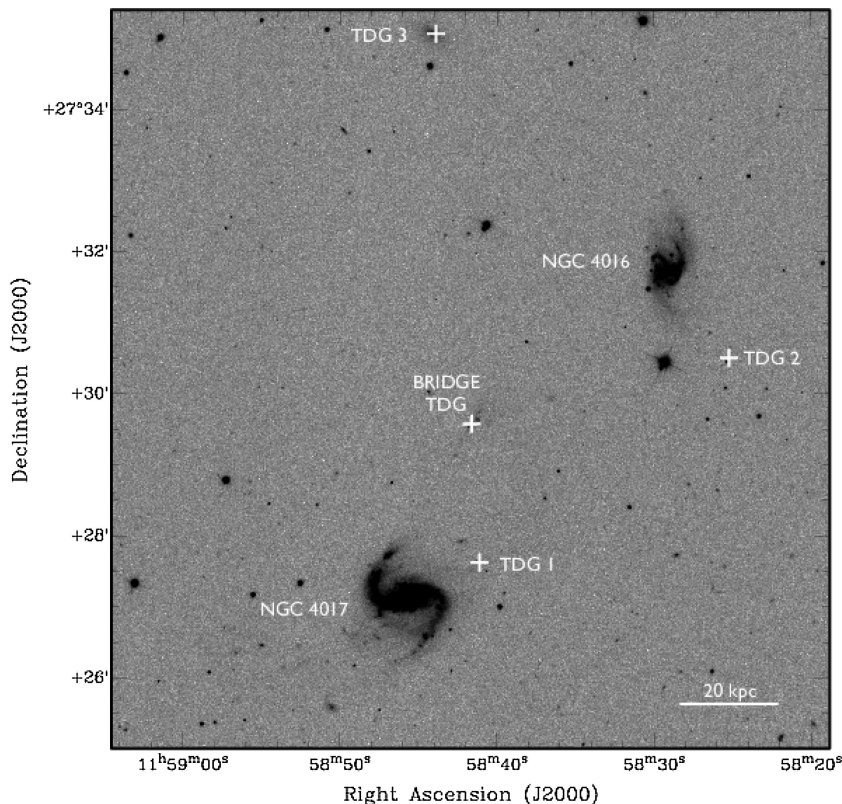


**Figure 1.** Arp 305: SDSS *g*-band image, with the positions of the two principal galaxies, NGC 4016 and NGC 4017, indicated, as well as the positions of the four TDG candidates from Hancock et al. (2009).

**Table 2.** GMRT observation details.

Frequency	1420.4057 MHz
Observation date	2014 July 12
Primary calibrator	3C147
Phase calibrator (flux density)	1120+143 (2.42 mJy)
Integration time	10.0 h
Primary beam	24 arcmin at 1420.4057 MHz
Low-resolution beam	$31.8 \times 29.5 \text{ arcsec}^2$ (PA = $-0^\circ:8$ )
High-resolution beam	$14.3 \times 11.8 \text{ arcsec}^2$ (PA = $27^\circ:8$ )
rms for low-resolution map	$1.2 \text{ mJy beam}^{-1}$
rms for high-resolution map	$0.6 \text{ mJy beam}^{-1}$
RA (pointing centre)	$11^{\text{h}} 58^{\text{m}} 37^{\text{s}}.4$
Dec. (pointing centre)	$27^\circ 29' 26''.9$

H I 21-cm line observations. The resultant velocity resolution was  $\sim 7 \text{ km s}^{-1}$ . Further details of the observations are given in Table 2.

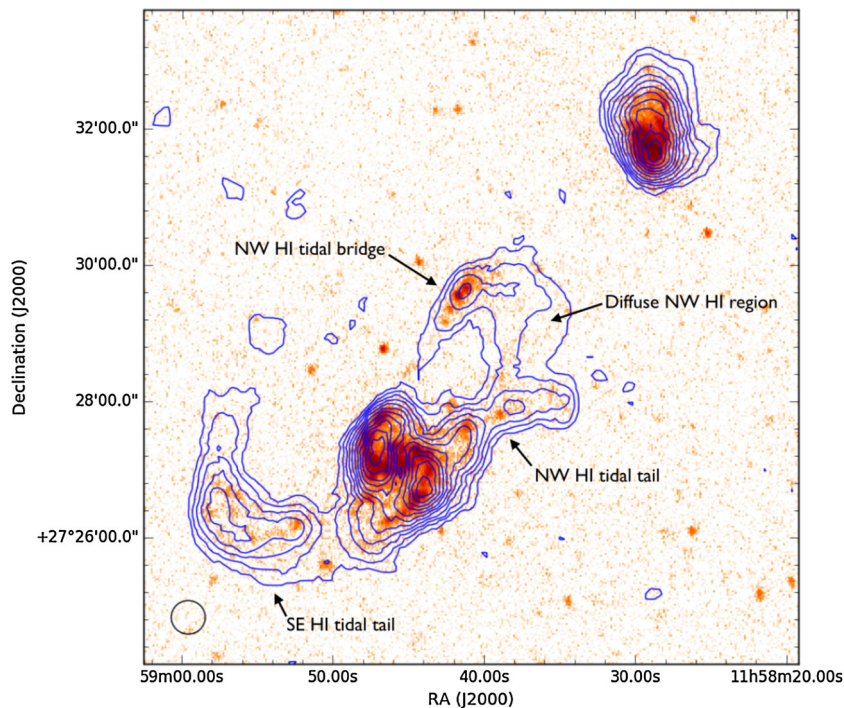
The AIPS (Astronomical Image Processing System) software package was used to reduce the data. Data from malfunctioning antennas, low-gain antennas and/or antennas suffering from radio frequency interference were flagged. The flux density calibration scale used was Baars et al. (1977), with flux density uncertainties  $\sim 5$  per cent. After calibration, the UV domain continuum subtraction was carried out using the AIPS task UVLIN. The task IMAGR was then applied to the visibilities to ‘clean’ and transform them into H I image cubes. The integrated H I, H I velocity field and velocity dispersion maps were made applying the AIPS task MOMNT on the H I cubes. To analyse the detailed H I morphology and kinematics, images with different resolutions were produced by applying different ‘tapers’ to the data with varying UV limits. Details of the final low- and high-resolution map properties are given in Table 2.

### 3 OBSERVATIONAL RESULTS

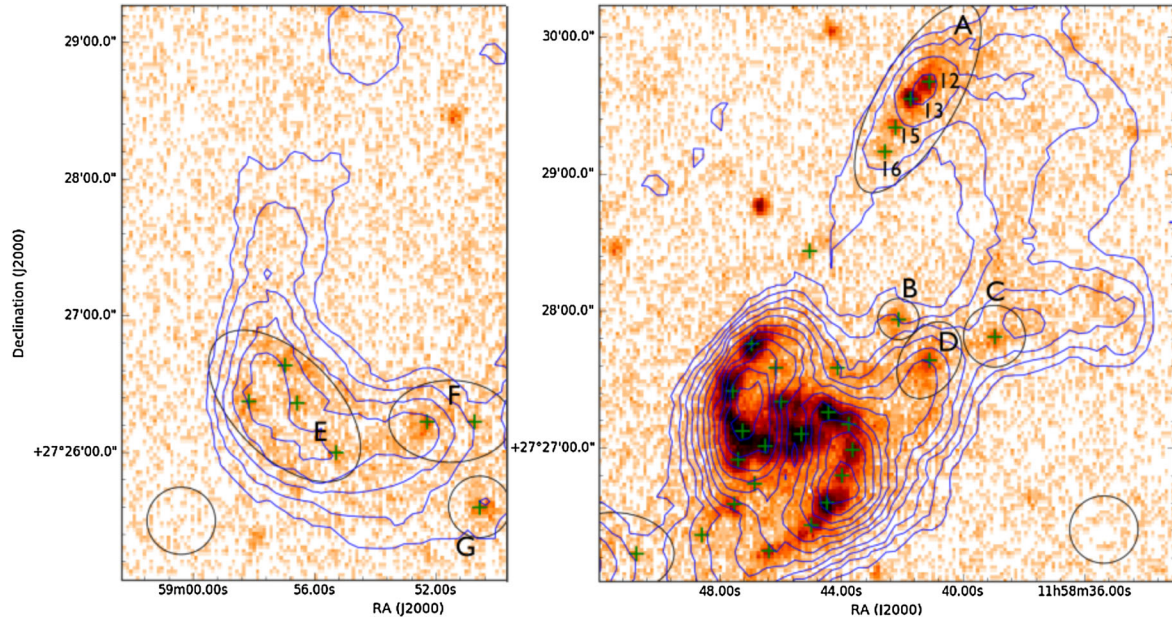
#### 3.1 H I morphologies and mass estimates

Fig. 2 shows the contours from the GMRT low-resolution ( $31.8 \times 29.5 \text{ arcsec}^2$ ) integrated H I map for the Arp 305 field overlaid on an FUV (*GALEX*) image, while Fig. 3 is a zoom in on the elaborate SF regions mainly outside the galaxy discs. The bulk of the H I is detected in NGC 4017, with significant amounts of its H I detected at lower column densities [ $(0.5\text{--}4.3) \times 10^{20} \text{ cm}^{-2}$ ] in an extended south-eastern (SE) tidal tail and a broad area north (N) and north-west (NW) of the optical disc. We refer to H I column densities as ‘lower’ or ‘higher’ with respect to the H I column density threshold of  $\sim 4 \times 10^{20} \text{ atoms cm}^{-2}$  for SF, as estimated by Maybhatte et al. (2007).

To a first order, the morphologies and the peak H I column densities of both members of the Arp 305 pair in the GMRT low-resolution (synthesized beam  $\sim 31.8 \times 29.5 \text{ arcsec}^2$ ) and lower resolution WSRT (van Moorsel 1983) (synthesized beam  $\sim 45 \times 60 \text{ arcsec}^2$ ) H I maps are similar. Although, it is evident from a comparison of the GMRT and WSRT H I morphologies that the GMRT has suffered some flux loss due to a lack of short-spacing baselines. For NGC 4016, Fig. 2 shows that its H I is truncated in the south to approximately the optical disc radius with the H I column densities rising rapidly towards the column density maximum. In the north, the H I disc extends beyond the optical disc. No H I counterparts to TDG 2 and TDG 3 were detected by the GMRT. In the case of NGC 4017, Fig. 2 shows massive extended H I tidal tails SE and NW of the galaxy’s FUV disc. The SE tidal tail (henceforth the ‘SE H I tidal tail’) contains high column density H I, within which are projected several SF clumps detected in UV. To the north (N) and north-west (NW) of the NGC 4017 optical disc, the H I morphology is more complex. Fig. 2 shows that it contains



**Figure 2.** Arp 305: integrated H I contours from the GMRT low-resolution map overlaid on an FUV (*GALEX*) image. The H I column density contour levels are  $N_{\text{H I}} = 10^{20} \text{ atoms cm}^{-2}$  (0.5, 1.7, 2.9, 4.1, 5.3, 6.4, 8.8, 11.1, 12.9). Major H I tidal features referred in the text are marked. The ellipse at the bottom left-hand panel shows the size of low-resolution ( $31.8 \times 29.5 \text{ arcsec}^2$ ) synthesized beam.



**Figure 3.** NGC 4017 zoom-in on the low-resolution integrated H I map contours overlaid on an FUV (*GALEX*) image. Left-hand panel: SE H I tidal tail. Right-hand panel: NW H I tidal tail and NW H I tidal bridge regions of NGC 4017. The green crosses mark the positions of the UV clumps from Hancock et al. (2009), with the black ellipses marking the SF zones A–G. For SF zone A (the bridge TDG), the (Hancock et al. 2009) FUV clump number is also indicated. The H I contour details are as per Fig. 2. The ellipses at the bottom of the figures indicate the GMRT low-resolution synthesized beam ( $31.8 \times 29.5$  arcsec<sup>2</sup>).

**Table 3.** GMRT H I detections.

Object	RA (h:m:s)	Dec. (d:m:s)	Velocity <sup>a</sup> (km s <sup>-1</sup> )	$W_{20}$ <sup>a</sup> (km s <sup>-1</sup> )	$M_{\text{H I}}$ <sup>b</sup> ( $\times 10^9 M_{\odot}$ )	$M_*$ <sup>c</sup> ( $\times 10^6 M_{\odot}$ )	FUV clumps <sup>c</sup>
Arp 305 pair:							
NGC 4016	11:58:29.0	+27:31:44	$3454 \pm 7$	$130 \pm 7$	3.0	10 400	1–10
NGC 4017	11:58:45.7	+27:27:09	$3439 \pm 7$	$258 \pm 7$	5.0	33 900	11, 14, 17, 18, 20–45
Bridge TDG candidate	11:58:42.22	+27:29:20.44	$3500 \pm 7$	$30 \pm 7$	0.66	1–7	12, 13, 15, 16

<sup>a</sup>From GMRT.

<sup>b</sup> $M(\text{H I})$  for NGC 4016 and NGC 4017 are derived from the GMRT flux densities. But see the caveats for the H I flux densities measured from GMRT as well as those found in the literature in Section 3.1. For the bridge TDG, the H I mass was calculated as per Section 4.3. The other H I detected candidate, TDG 1, is a small UV clump embedded in a much larger mass of H I debris close to the NGC 4017 disc. Its H I mass was not estimated due to the high uncertainties in its extent and the corresponding flux density.

<sup>c</sup>From table 5 in Hancock et al. (2009), except for the  $M_*$  masses of NGC 4016 and NGC 4017 that were calculated using the method from Bell et al. (2003) and parameters from Blanton et al. (2003) based on the galaxies’ SDSS *r*-band magnitudes and *r*–*i* colours.

two elongated H I structures of relatively high column density with FUV counterparts. The first structure is an H I extension, with a clumpy FUV counterpart, including TDG 1, running from the western edge of the optical/FUV disc to the NW (henceforth the ‘NW H I tidal tail’). The second prominent H I structure is the H I counterpart to the UV and optical tidal bridge remnant between NGC 4017 and NGC 4016, referred to from here on as the ‘NW H I tidal bridge’. The bridge TDG candidate is projected within the NW H I tidal bridge. Both of these large-scale H I structures, also visible in the WSRT map, are embedded within a much more extensive lower H I column density region, which in the WSRT map extends  $\sim 1.5$  arcmin (22 kpc) farther north than in the GMRT map, almost connecting to the NGC 4016 H I disc. This region is referred to as the ‘diffuse NW H I region’. Properties of the two principal galaxies and the TDG candidates, including their GMRT H I masses as well as their velocities and  $W_{20}$  linewidths, are set out in Table 3.

Comparing the H I masses for NGC 4016 and NGC 4017 derived from the GMRT to their literature H I flux densities is complicated by the following factors: (i) There are conflicting H I flux densities reported in the literature for the galaxies from several single-dish and

a single-WSRT interferometric observation (van Moorsel 1983). (ii) The close proximity of NGC 4016 and NGC 4017 and large single-dish beam sizes mean that H I emission is likely to be partially confused within the single-dish beams. Only the GMRT and WSRT H I maps resolve NGC 4016 and NGC 4017 into discrete H I entities. (iii) It is difficult to accept that the WSRT flux calibration was accurate because the 1.4-GHz WSRT radio continuum flux density for NGC 4016 was  $\sim 1.5$  times the NRAO VLA Sky Survey (NVSS) value, but for NGC 4017, the WSRT radio continuum flux density is similar to the NVSS value. (iv) As noted above, comparison of the WSRT and GMRT H I maps indicates that the GMRT observation did suffer some flux loss. Below we compare the GMRT and literature H I flux densities values for NGC 4016 and NGC 4017.

The GMRT integrated H I flux density ( $S$ ) for NGC 4016 was  $S = 5.0$  Jy km s<sup>-1</sup> compared to  $S = 7.5$  Jy km s<sup>-1</sup> from the van Moorsel (1983) WSRT H I mapping. Single-dish flux density measurements for NGC 4016 have been reported:  $S = 10.05$  Jy km s<sup>-1</sup>, using the 305-m Arecibo telescope (Haynes et al. 2011); and  $S = 8.1$  Jy km s<sup>-1</sup>, from the Nançay radiotelescope (Theureau

et al. 2007); and  $6.2 \text{ Jy km s}^{-1}$ , from the Arecibo telescope (Huchtmeier & Richter 1989). The Nançay beam is quite large [full width half power (FWHP),  $3.6 \times 22 \text{ arcmin}^2$  at zero declination]. Assuming that the Nançay observation was centred on NGC 4016, the flux density derived in Theureau et al. (2007) would be contaminated with emission from NGC 4017, with the severity depending on the size and orientation of the beam. Arecibo’s beam has an FWHP  $\sim 3.5 \text{ arcmin}$ . Haynes et al. (2011) note that the H I emission detected with Arecibo at the position of NGC 4016 is ‘probably’ blended with emission from NGC 4017, and their reported flux density for NGC 4016 is after ‘attempted’ deblending. Since the H I flux values reported in the literature were so diverse, we compared our GMRT 20-cm radio continuum flux value of NGC 4016 ( $5.3 \text{ mJy} \pm 10 \text{ per cent}$ ) with that from the NVSS ( $5.5 \text{ mJy} \pm 10 \text{ per cent}$ ) as a check for our GMRT calibration. These matching continuum values indicate that our calibration is accurate and the literature H I flux densities that differ widely from the GMRT value for NGC 4016 cannot be accepted as reliable measurements.

For NGC 4017, the GMRT integrated interferometric flux density is  $S = 8.5 \text{ Jy km s}^{-1}$ , compared to  $S = 25.8 \text{ Jy km s}^{-1}$  from the WSRT (van Moorsel 1983). In part, the difference is attributable to the GMRT H I flux loss referred to above, and the similarity of the peak H I column densities in the WSRT and GMRT maps is consistent with this. However, the NGC 4017 van Moorsel (1983) H I flux density ( $S = 25.8 \text{ Jy km s}^{-1}$ ) is in good agreement with that derived by Haynes et al. (2011) from Arecibo single-dish observations. But, Haynes et al. (2011) note the possible blending of H I emission from NGC 4016. A significantly lower Arecibo-based H I flux density for NGC 4017 of  $S = 16.8 \text{ Jy km s}^{-1}$  is reported in Lewis, Helou & Salpeter (1985). The NGC 4017 H I extent is greater than a single Arecibo  $\sim 3.5$ -arcmin beam, thus requiring integration of the flux densities from multiple pointings. But neither Haynes et al. (2011) nor Lewis et al. (1985) state which beam areas were used to derive their reported NGC 4017 flux densities.

Compared to the GMRT H I flux density, the NGC 4017 flux densities from Haynes et al. (2011) and van Moorsel (1983) are about three times higher. While some flux loss is expected in GMRT data due to the lack of short baselines, the flux loss of  $\sim 60 \text{ per cent}$  implied by the Haynes et al. (2011) and van Moorsel (1983) flux densities is much higher than expected, based on similar GMRT observations. Furthermore, the ‘expected’ H I mass of a galaxy of NGC 4017’s size and Hubble type, based on a large sample of field galaxies and using the formula from Haynes & Giovanelli (1984) ( $M_{\text{HI}} = 4.1 \times 10^9 M_{\odot}$ ), is in good agreement the H I mass derived from the GMRT ( $M_{\text{HI}} = 4.8 \times 10^9 M_{\odot}$ ). The NGC 4017 H I mass derived from Haynes et al. (2011) and van Moorsel (1983) flux densities are also significantly higher than the H I mass derived from applying the Tully–Fisher (TF) relations. Our stellar mass estimate for NGC 4017 of  $3.0 \times 10^{10} M_{\odot}$  agrees well with the stellar TF mass relation, based on an H I rotation velocity of  $\sim 201 \text{ km s}^{-1}$  ( $150 \text{ km s}^{-1}$  from the rotating disc adjusted for inclination). But using the NGC 4017 H I flux density from Haynes et al. (2011) and assuming molecular mass = H I mass gives a baryonic mass of  $6.6 \times 10^{10} M_{\odot}$ , significantly greater than the baryonic mass for NGC 4017 from the TF baryonic mass relation ( $3.8 \times 10^{10} M_{\odot}$ ). The TF baryonic mass relation is a tighter relation than the stellar TF according to Torres-Flores et al. (2011). Hence, the NGC 4017 H I masses from the ‘expected’ and TF analysis are closer to those derived from the GMRT and Lewis et al. (1985) H I flux densities than those derived from the Haynes et al. (2011) and van Moorsel (1983) flux densities. We conclude that the greater extent of the H I detection in the van Moorsel (1983) map clearly shows that the

GMRT data are missing some flux. But large uncertainties about reliability of the flux densities in the literature prevent us from quantifying the amount of this loss. Analysis in this paper, however, concentrates on the relatively compact, high-density H I SF zones where flux loss should not affect any of our results significantly.

### 3.2 H I kinematics

Fig. 4 shows the low-resolution ( $\sim 30 \text{ arcsec}$ ) intensity-weighted velocity field of the Arp 305 system, with iso-velocity contours separated by  $7 \text{ km s}^{-1}$ . For NGC 4016, H I emission is detected in the channel maps (Figs 8 and 9) within a velocity range  $3348\text{--}3496 \text{ km s}^{-1}$ . The NGC 4016 iso-velocity contours (Fig. 4) indicate reasonably regular rotation in the H I disc, with a north–south (N–S) kinematic axis. The closed iso-velocity contours at the H I disc edges indicate that the disc is warped with the velocity gradient becoming progressively shallower towards the north. NGC 4016 has a GMRT  $V_{\text{HI}} = 3454 \pm 7 \text{ km s}^{-1}$ , with  $W_{20} \sim 130 \pm 7 \text{ km s}^{-1}$ , close to  $W_{50} \sim 133 \pm 15 \text{ km s}^{-1}$  from the single-dish online data from Haynes et al. (2011).

In the channel maps (Figs 8 and 9), H I emission is detected for NGC 4017 in the velocity range  $3292\text{--}3595 \text{ km s}^{-1}$ . Its GMRT  $V_{\text{HI}} = 3439 \pm 7 \text{ km s}^{-1}$  agrees well with the heliocentric optical radial velocity for NGC 4017 ( $3449 \pm 2 \text{ km s}^{-1}$ ). The GMRT  $W_{20} = 258 \pm 7 \text{ km s}^{-1}$  is also similar to  $W_{50} = 253 \pm 5 \text{ km s}^{-1}$  from single-dish online data (Haynes et al. 2011). The NGC 4017 iso-velocity contours in the H I velocity field (Fig. 4) also show a fairly regular rotation pattern ( $\text{PA} = 111^\circ$ ). A position velocity (PV) diagram for a cut along the NGC 4017 major axis (Fig. 6) shows the H I line centre to be  $3447 \pm 7 \text{ km s}^{-1}$  and maximum rotation velocity to be  $\sim 150 \pm 7 \text{ km s}^{-1}$  (before inclination correction). Two structures in the NGC 4017 PV diagram (see Fig. 6 – right-hand panel) with offsets  $> +0.6 \text{ arcmin}$  and  $< -1.0 \text{ arcmin}$ , respectively, are cuts through the SE and NW H I tidal tails. The velocities in the SE H I tidal tail, which, in projection, is an extension of the southern optical spiral arm, initially systematically decreases along the tail to a velocity  $\sim 115 \text{ km s}^{-1}$  below the NGC 4017 systemic velocity, at which position the projected direction begins changing northwards. Beyond this position, the H I tail velocities systematically increase reaching the NGC 4017 systemic velocity at the end of the H I tail. To the NW of NGC 4017, from the base of the NW H I tidal tail, the H I velocities increase systematically along the NW H I tidal tail all the way to the NW H I tidal bridge. Along the NW H I tidal bridge itself, H I velocities decline systematically in the direction of NGC 4017. There is no clear kinematic break to distinguish the NW H I tidal tail, diffuse NW H I region and the NW H I tidal bridge. In fact, the kinematic continuity from NW H I tidal tail through the diffuse NW H I region to NW H I tidal bridge is puzzling. Modelling by Hancock et al. (2009) of the Arp 305 system predicts the NW tidal bridge, but the origin of the NW H I tidal tail and diffuse NW H I region is unclear. The authors attribute them to ‘material splashed out of the discs at closest approach’. However, in terms of H I mass, column density as well as kinematics, the NW H I tidal tail appears to be an equally unambiguous and robust structure as the NW H I tidal bridge.

Overall, the H I morphology and kinematics for NGC 4017 suggest multiple H I structures in NGC 4017: (i) a regular rotating H I disc with a similar inclination to the optical galaxy ( $48^\circ$ ) and  $\text{PA} \sim 111^\circ$ ; (ii) an SE H I tidal tail; (iii) an NW H I tidal tail; (iv) the NW H I tidal bridge counterpart, which is distinguishable by its local column density peak, although, not kinematically; and (v) the extensive diffuse NW H I region, which is not clearly

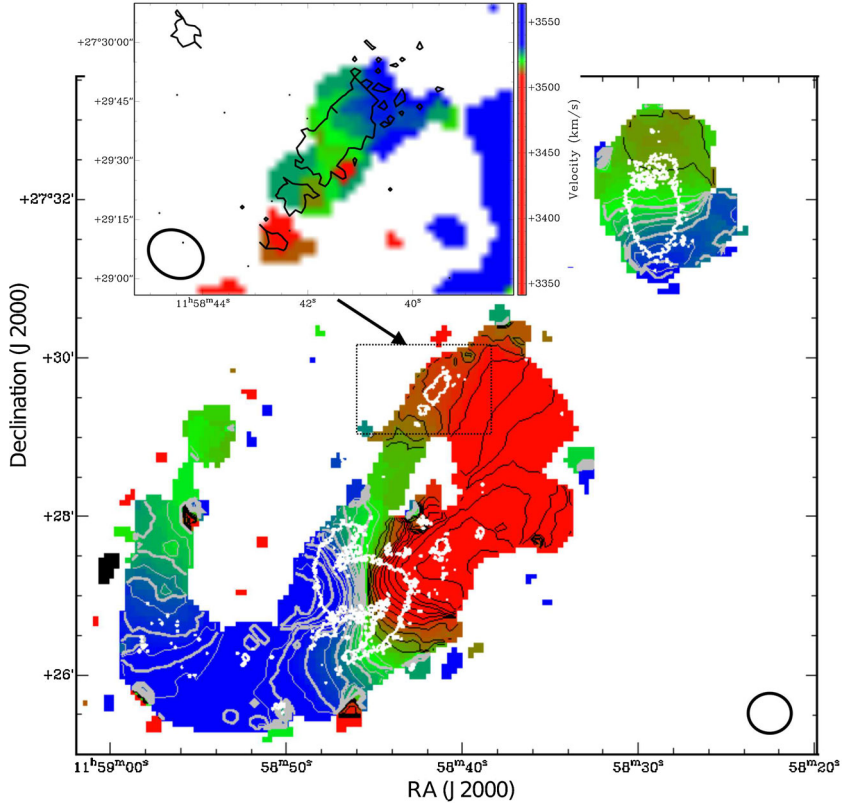


**Figure 4.** Arp 305: main figure: H I velocity field from the GMRT low-resolution cube for H I emission  $>3\sigma$ . The areas in red with black contours have velocities greater than the NGC 4017 systemic velocity of  $3439 \text{ km s}^{-1}$ , and areas in blue with grey contours have velocities  $<3439 \text{ km s}^{-1}$ . The contours are in steps of  $7 \text{ km s}^{-1}$ . The thick white contour is from the FUV (*GALEX*) image. The GMRT low-resolution beam ( $31.8 \times 29.5 \text{ arcsec}^2$ ) is shown in the bottom right-hand corner. Inset: zoom-in on the bridge TDG region showing the velocity field of the GMRT high-resolution H I cube for emission  $>3\sigma$ . The GMRT high-resolution beam ( $14.3 \times 11.8 \text{ arcsec}^2$ ) is shown in the bottom left-hand corner.

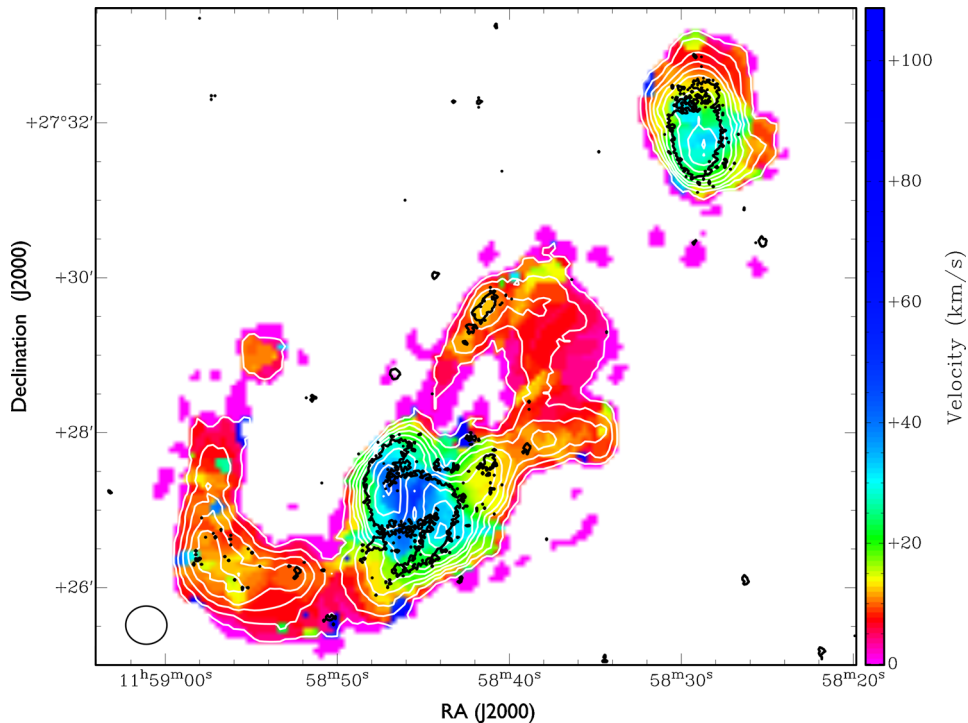


**Figure 5.** Arp 305: GMRT velocity dispersion map from the low-resolution cube. The white contours are from the low-resolution H I integrated map (Fig. 2). The ellipse at the bottom left-hand panel indicates the GMRT-synthesized beam ( $31.8 \times 29.5 \text{ arcsec}^2$ ).

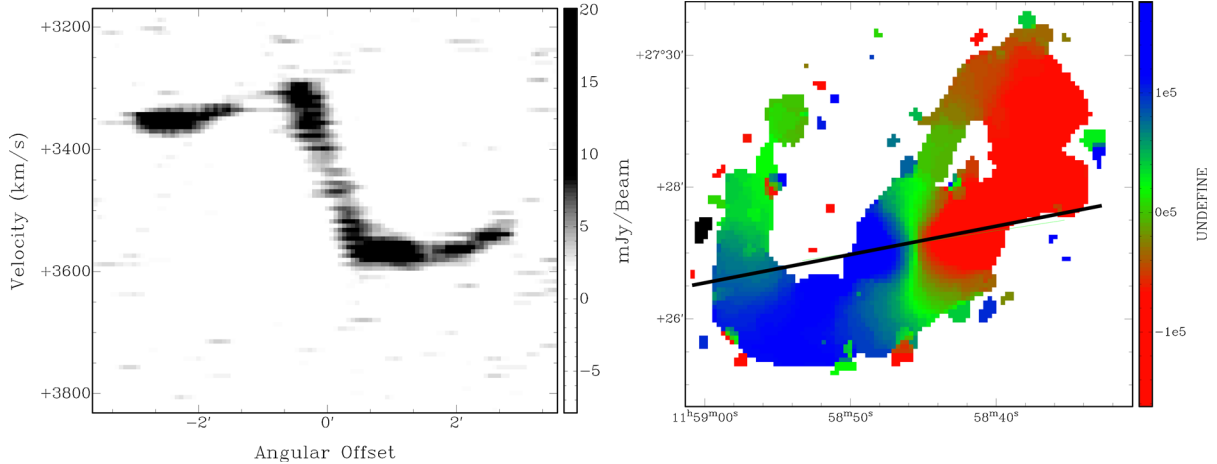


**Figure 6.** NGC 4017 PV diagram. Left-hand panel: PV diagram at PA  $291^\circ$ . Positive angular offset values are to the NW of the kinematic centre and negative values are to the SE, with the angular offset scale in arcminutes. Right-hand panel: GMRT NGC 4017 H I velocity field showing the position of the PV cut in the left-hand panel.

distinguishable as a separate kinematic structure from the H I bridge or the NW tidal tail.

## 4 DISCUSSION

### 4.1 Interaction dynamics

Since the most recent NGC 4017–NGC 4016 interaction in H I, Arp 305 has shown strong tidal interaction signatures, including the SE H I tidal tail, NW H I tidal tail and NW H I tidal bridge. Arp 305 specific modelling for a prograde interaction by Hancock et al. (2009) predicted stellar counterparts to the SE H I tidal tail for NGC 4017 and the NW tidal bridge between the pair. Both tidal features are also predicted by generalized modelling of a late-type galaxy undergoing a prograde interaction with a minor companion (Oh et al. 2008). However, Arp 305 also exhibits extended H I debris (i.e. the NW H I tidal tail and the diffuse NW H I region) that is not predicted by either the Hancock et al. (2009) or Oh et al. (2008) models. The fact that these features are seen in H I and are bright in UV, but lack optical counterparts, suggests that these features are young interaction debris. H I kinematic and morphology perturbations in the GMRT maps are more severe on the western side of the NGC 4017 disc, indicating NGC 4016’s closest approach occurred there. A possible explanation for the NW H I tidal tail is that it was H I tidally drawn out of the NGC 4017 disc during the pericentre approach of NGC 4016. Hancock et al. (2009) attribute this structure (NW H I tidal tail) to the material ‘splashed out’ during NGC 4016’s closest approach. However, in terms of H I mass, column density as well as kinematics, the NW H I tidal tail is as well defined a structure as the NW H I tidal bridge. Additionally, the diffuse NW H I region in the WSRT map, which is only partially recovered by the GMRT map, has an enormous extent. Also, the continuous kinematic gradient from the NW H I tidal tail along the kinematic major axis of NGC 4017 (Fig. 3) until it merges with the NW H I tidal bridge is inconsistent with the disturbed kinematics expected in ‘splashed-out’ debris. In the absence of a better model, we, of course, cannot make any robust claim. Alternative explanations could be that (i) the NW H I tidal tail is a tidal feature attributable to the close approach of NGC 4016 on that side of the galaxy, and (ii) at least part of the diffuse NW H I region is H I debris from an earlier encounter between the pair. Similar massive H I structures have been previously

reported in M 51-type systems, which could not be explained by modelling of a single encounter and were speculated to originate from multiple passage encounters (Howard & Byrd 1990; Salo & Laurikainen 1993).

Oh et al. (2008) used simulations to study the enhancement of the spiral features and the duration of visibility in disc galaxies following an interaction with a perturber. The similarity in the baryonic masses of NGC 4017 ( $\sim 4.0 \times 10^{10} M_\odot$ ) and the disc galaxy used in the Oh simulations ( $\sim 5.2 \times 10^{10} M_\odot$ ) allows us to use the Oh et al. (2008) model to understand the physical properties of NGC 4017 (acknowledging that the NGC 4017 orbital parameters are poorly constrained in comparison with the Oh simulations). To access the strength of the tidal interaction between simulated galaxy pairs and understand interactions with  $S < 0.3$ , i.e. moderately strong interactions, Oh et al. (2008) used a tidal strength parameter:  $S = \left(\frac{M_p}{M_g}\right) \left(\frac{R_g}{R_{\text{peri}}}\right)^3 \left(\frac{\Delta T}{T}\right)$  (their equation 3). We can estimate, for NGC 4017, the perturber-to-galaxy mass ratio ( $\frac{M_p}{M_g}$ ) at  $\sim 3$ , a typical value for interacting pairs with TDGs. For NGC 4017, we do not have any observational constraint for the pericentre to galaxy radius ( $\frac{R_g}{R_{\text{peri}}}$ ) ratio or the perturber angular speed relative to stars at the galaxy edge ( $\frac{\Delta T}{T}$ ). Additionally, the Oh et al. (2008) simulations reveal that the tidal tails dissipate rapidly after reaching their visibility maximum, i.e.  $(1.4\text{--}2.5) \times 10^8$  yr following the interaction. For  $S > 0.3$  interactions, the time-scale for tail dissipation may extend to  $\sim 1$  Gyr and tail fragmentation may lead to TDG formation (Barnes 1992; Oh et al. 2008). Here, using the Oh models as well as other observational evidence, we make an effort to constrain the time since the most recent NGC 4017–NGC 4016 interaction. Following are our four sources of evidence: (i) For galaxies with total baryonic masses of the order of NGC 4017, H I morphological perturbation signatures from a full merger remain identifiable only for a maximum of  $\sim 4 \times 10^8\text{--}7 \times 10^8$  yr (Holwerda et al. 2011). We find the H I morphology in NGC 4017 to be strongly disturbed, i.e. well above the Holwerda H I merger signature threshold. Assuming H I perturbations from a full merger would be of a similar magnitude to the pre-merger interaction observed in NGC 4017, it seems reasonable to conclude that the NGC 4017 perturbation occurred well within the Holwerda et al. (2011) time-scale upper limits. (ii) NGC 4016 and NGC 4017 have a projected separation of 372 arcsec (90 kpc). If we assume a separation velocity of  $\sim 212$  km s $^{-1}$ ,

i.e. twice the USGC U435 group velocity dispersion, it implies that the time since their closest approach was  $\sim 4.1 \times 10^8$  yr. (iii) Using an inclination-corrected rotational velocity of  $201 \text{ km s}^{-1}$ , the time for a single rotation<sup>2</sup> of NGC 4017 is  $\sim 0.6 \times 10^9$  yr. Following the Oh et al. (2008) simulations, we make the assumption that the bridge was formed along an axis joining NGC 4016 to NGC 4017 at the time of their closest approach, and this point of closest approach has since rotated and reached its current location. From the orientation of the system and its H I morphology and kinematics, it seems that the point of closest approach was the western edge of the NGC 4017 disc where the ‘splashed-out’ material is visible. Relative to the optical centre in an SDSS *g*-band de-projected image<sup>3</sup> of NGC 4017, the western disc edge is offset by  $\sim 262^\circ$  in an anticlockwise direction from the bridge. This implies that the NGC 4017 disc has rotated  $\sim 262^\circ$  since the bridge was formed, and we estimate the time since the bridge was formed at  $\sim 4 \times 10^8$  yr<sup>4</sup>. (iv) A comparison of the optical morphology of NGC 4017 and the Oh et al. (2008) simulations (their Fig. 1) shows a good agreement around  $t = 0.3$  and  $0.4$  Gyr. While the uncertainties for each of these time-scales are large, they sort of indicate that the interaction took place within the last  $\sim 4 \times 10^8$  yr. This time-scale agrees well with the  $3.8 \times 10^8$  yr from the Hancock et al. (2009) modelling. Even  $\sim 4 \times 10^8$  yr after the most recent pericentre approach, strong H I morphological and kinematic perturbation signatures from the interaction remain clearly observable. The prominent optical tidal features of NGC 4017 in this time frame is consistent with the Oh et al. (2008) simulations. This together with the presence of TDG candidates support an argument in favour of an  $S < 0.3$  interaction.

#### 4.2 SF and H I column densities

A rich array of SF activity in Arp 305 is indicated by the emission detected in UV (*GALEX*) images. Extended areas of SF are detected in FUV beyond the optical discs of both NGC 4016 and NGC 4017 (Fig. 2). Hancock et al. (2009) carried out a detailed study of SF in the tidal features of Arp 305 using UV (*GALEX*) data. Those authors identified 45 isolated SF clumps within the extragalactic tidal debris, including in four TDG candidates; see tables 3 and 4 of Hancock et al. (2009). For NGC 4017, we explore the relationship between the Hancock extragalactic FUV clumps and the H I debris in which they are projected, i.e. in the extended H I debris of the NW tidal tail, NW diffuse region and SE H I tidal tail, as marked in Fig. 3. Because of the GMRT’s lower spatial resolution ( $\sim 30$  arcsec) compared to UV data from *GALEX* ( $\sim 5$  arcsec), we study the aggregated SF behaviour in each of the zones marked A–G in Fig. 3. Table 4 sets out the H I column densities, SFR and FUV clumps within each SF region. As noted in Section 3.1, extragalactic tidal H I debris was detected at the projected positions of only two of the four TDG candidates. SF zones A and D correspond to the bridge TDG and TDG 1 candidates, respectively. Other SF zones projected within the H I debris are centrally concentrated SF clumps (zones B, C and G) and zones of multiple small faint clumps (zones E and F).

Hancock et al. (2009) note multiple strong SF sites over an extensive area of the SE H I tidal tail region, and their model of the Arp 305 interaction also predicts high gas densities in those strong SF regions of the SE H I tidal tail. Indeed, apart from the main galaxy discs of

**Table 4.** NGC 4017 SF zone properties.

Zone	ID	SFR ( $M_\odot \text{ yr}^{-1}$ )	H I column density ( $\times 10^{20} \text{ cm}^{-2}$ )	FUV clump <sup>a</sup>
A	Bridge TDG	0.200	4.1	12, 13, 15, 16
B		0.009	1.7	14
C	TDG 1	0.015	2.9	42
D		0.010	6.4	11
E		0.020	5.3	37, 38, 43, 40
F		0.011	4.1	39, 44
G		0.009	0.5	36

<sup>a</sup>From (Hancock et al. 2009).

NGC 4016/7, the SE H I tidal tail has highest GMRT H I column densities. However, the total SFR in the SE H I tidal tail ( $0.04 M_\odot \text{ yr}^{-1}$ ) is an order of magnitude lower than in the bridge TDG candidate ( $0.2 M_\odot \text{ yr}^{-1}$ ). The SF zones (A–G) are projected within H I with column densities ranging from  $0.5$  to  $6.4 \times 10^{20} \text{ cm}^{-2}$ . However, the H I local maxima are not necessarily spatially correlated with the individual SF zones. It is worth mentioning here that several studies have been conducted in the past to ascertain the critical H I column density that triggers SF in galaxies as suggested by Kennicutt (1989). Earlier studies, for example, Skillman et al. (1988), found the limit to be  $\sim 10^{21} \text{ cm}^{-2}$  (for a spatial resolution of 500 kpc). A more recent study in the outskirts of the main galaxy discs and tidal debris found the limit to be  $\sim 4 \times 10^{20} \text{ cm}^{-2}$  over a spatial resolution of about 1 kpc (Maybhathe et al. 2007). The spatial resolution plays a crucial role as the quoted H I column density values can change with the synthesized beam size. In the case of Arp 305, the spatial resolutions we reach are  $\sim 7$  kpc with the low-resolution map and  $\sim 3$  kpc with the high-resolution map. While this prevents us from drawing any firm conclusion about SF, above or below the critical column density regions in the Arp 305 system, the wide range of H I column density regions hosting SF in Arp 305 reaffirms that a critical H I column density may be a necessary criteria but not a sufficient one to initiate SF (Begum et al. 2006).

Areas of higher velocity dispersion in the extragalactic H I debris in the GMRT H I velocity dispersion map (Fig. 5) correlate well with the SF zones (A–G). For the SF zones projected within the SE and NW H I tidal tails and NW H I tidal bridge, the velocity dispersion values range between 10 and  $15 \text{ km s}^{-1}$ , higher than the usual  $7\text{--}8 \text{ km s}^{-1}$  in the non-SF areas of the extragalactic H I debris. Within the optical discs of the two galaxies, H I velocity dispersions are higher, i.e.  $\sim 15\text{--}40 \text{ km s}^{-1}$ . This is consistent with Mullan et al. (2013), who found that compact star clusters in H I tidal tails are preferentially located in H I regions with column densities  $> 4.6 \times 10^{20} \text{ cm}^{-2}$  (1 kpc resolution) and the highest H I velocity dispersions. Mullan et al. (2013) also argue that higher H I velocity dispersion is a condition for SF in the tidal tails, rather than consequence of the SF. The star formation rates (SFRs), estimated from the FUV fluxes (Hancock et al. 2009) for the SF zones A–G, are 0.2, 0.009, 0.015, 0.010, 0.020, 0.011 and  $0.009 M_\odot \text{ yr}^{-1}$ , respectively. The highest SFR in zone A contains the bright SF bridge TDG candidate, consisting of four strong SF clumps. The bridge TDG candidate is discussed further in Section 4.3.

#### 4.3 Arp 305 bridge TDG candidate

Validation of a TDG candidate usually requires a combination of evidence linking the candidate to the interaction between its parents, its metallicity, its stellar population and gas disc rotation

<sup>2</sup>  $T_{\text{rot}}$  (Gyr) =  $6.1478 r/V_{\text{rot}}$ , where  $r$  = the optical radius (kpc) and  $V_{\text{rot}} = 0.5 \Delta V$  ( $\text{km s}^{-1}$ )/ $\sin(i)$ .

<sup>3</sup> Based on PA =  $111^\circ$  and inclination =  $48.2^\circ$ .

<sup>4</sup>  $262^\circ/360^\circ \times 0.6 \times 10^9 \text{ yr} = 4 \times 10^8 \text{ yr}$ .

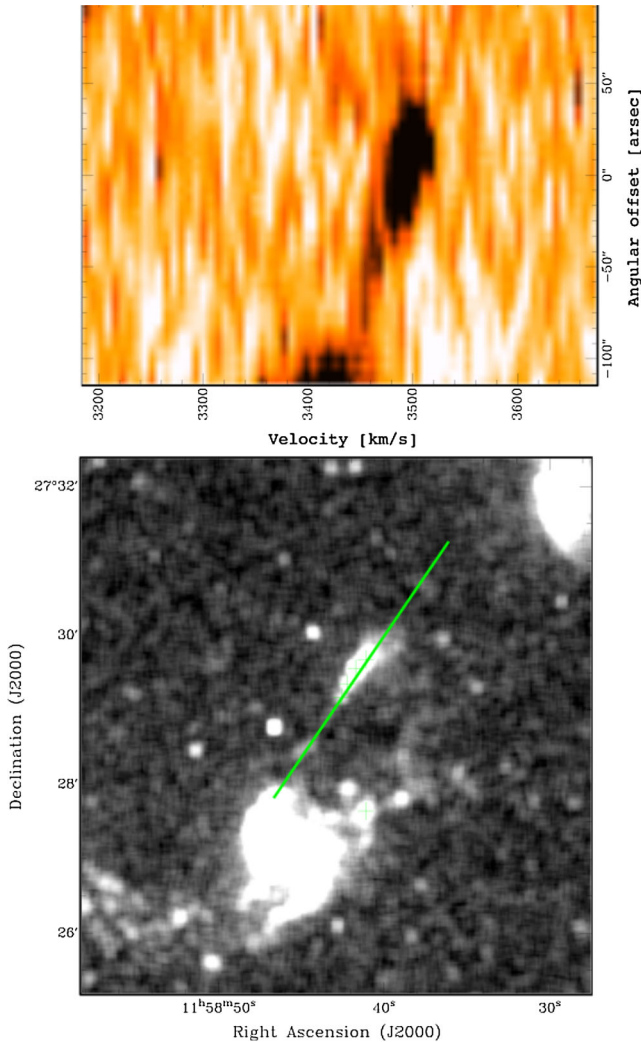


**Figure 7.** Bridge TDG PV diagram. Top panel: PV diagram cut from the low-resolution cube along the axis of the four FUV knots in the bridge TDG. Negative angular offsets are in the SE direction. Bottom panel: FUV image (*GALEX*) showing the position of the PV cut (PA  $146^\circ$ ) shown in the top panel.

signatures from H I, CO or H $\alpha$  velocity fields. The bridge TDG candidate emits strongly at UV wavelengths and has one of the bluest FUV-*g* colours ( $\sim 0.25$ ) amongst TDGs in the TDG sample studied by Schechtman-Rook & Hess (2012), indicating strong recent SF. Within the NW H I tidal bridge, the H I column density maximum in the low-resolution map ( $4.1 \times 10^{20}$  atoms  $\text{cm}^{-2}$ ) is projected at the position of the UV clumps 12 and 13 from Hancock et al. (2009) (see Fig. 3 – right-hand panel). An H I spectrum for the bridge TDG was extracted from the low-resolution cube, centred on its H I column density maximum, which includes the projected positions of the four Hancock UV clumps (numbered 12, 13, 15 and 16). This spectrum provides an upper limit for the H I mass of the bridge TDG ( $\sim 6.6 \times 10^8 M_\odot$ ). The velocity field and a PV diagram cut from the low-resolution cube, taken along the ‘tidal bridge’ major axis (Fig. 7), shows H I detected in the range 3475–3520  $\text{km s}^{-1}$  with a modest gradient and velocities increasing in the NW direction. The bridge TDG’s  $V_{\text{H I}} = 3500 \pm 7 \text{ km s}^{-1}$  is in good agreement with the velocities of the parent galaxies. The velocity gradient is also clearly seen in the high-resolution velocity field

(inset in Fig. 4). The PV diagram, the channel maps (Figs 8 and 9) and the H I map (Figs 2 and 3) reflect the concentration of H I along the major axis of the tidal bridge in the vicinity of UV clumps 12, 13, 15 and 16, with the highest H I column density at the projected position of UV clumps 12 and 13. There are also local maxima for velocity dispersion of  $\sim 14 \text{ km s}^{-1}$  at this position (Fig. 5).

In optical/UV images, the bridge TDG has an  $\sim 11$  kpc length and the low- and high-resolution GMRT synthesized beams ( $\sim 32$  and  $\sim 14$  arcsec) sample it at  $\sim 7$  and 3 kpc, respectively. The spectrum shows an H I linewidth of  $\sim 30 \text{ km s}^{-1}$  with a systematic gradient over  $\sim 50 \text{ km s}^{-1}$  across its major axis, with the velocity resolution being  $\sim 7 \text{ km s}^{-1}$ . These values agree well with those TDGs reported in the literature, for which a velocity gradient has been determined. In a recent work, Lelli et al. (2015) found signs of regular velocity gradient in six bona fide TDGs. Using a velocity resolution of 7–10  $\text{km s}^{-1}$  and a spatial resolution of about two to three beams across the major axis, they report gradients between 25 and 80  $\text{km s}^{-1}$ . A similar H I velocity gradient of  $\sim 30$ –40  $\text{km s}^{-1}$  was reported for a TDG candidate in the Leo triplet (Nikiel-Wroczyński et al. 2014). While the H I linewidth and velocity gradient estimates for the bridge TDG are consistent with those found in the literature, it remains unclear whether the velocity gradient represents the intrinsic rotation of the bridge TDG, or just the gradient within the H I debris.

Using the H I spectrum from the low-resolution cube for the bridge TDG, we estimated its dynamical mass ( $M_{\text{dyn}}$ ) to be  $7 \times 10^8 M_\odot$ . Based on their best-fitting models and scaling to the SDSS *r*-band flux, the stellar mass of the bridge TDG was estimated at  $(1\text{--}7) \times 10^6 M_\odot$  by Hancock et al. (2009), giving an  $\frac{M_{\text{H I}} + M_\star}{M_{\text{dyn}}}$  ratio of  $\sim 1$ . This ratio is consistent with the absence of a substantial dark matter component and is typical of the ratio found for validated TDGs. However, the following factors together make the estimate highly uncertain: (i) The TDG is embedded in an H I debris, and thus its spectrum can be contaminated by foreground and background emission. (ii) It is impossible to distinguish the extent of the H I disc of the TDG from the general bridge emission. (iii) Assuming that the bridge TDG was formed during the last encounter between the pair ( $\sim 4 \times 10^8 \text{ yr}$ ), it seems probable that there has been insufficient time for the bridge TDG to virialize (Flores et al. 2016). All these factors make the calculated  $M_{\text{dyn}}$  highly uncertain, and therefore while we present our estimates here, we choose not to make any strong claims on the dark matter content of the TDG based on it.

The Hancock et al. (2009) model of the stellar component of the pair interaction shows the development of a tidal bridge between NGC 4017 and NGC 4016, with SF activity near the centre of the bridge and the bridge base near NGC 4017. The authors suggest that ‘material balanced between the two galaxies’, NGC 4017 and NGC 4016, collapsed under its own gravity and gave rise to the TDG, i.e. the stellar debris provided the seed for accumulation and of gas debris that, in turn, fuelled SF in the TDG. Potentially, a kinematic rotation signature could confirm a TDG candidate as an independent galaxy, rather than just an accumulation of SF zones. However, in this case, this is not feasible as the bridge TDG is embedded in the bridge H I debris and the GMRT spatial resolution is too poor to distinguish the TDG candidate’s intrinsic kinematics from the kinematics of the H I debris. Due to their relatively higher metallicity than standard dwarf galaxies, the probability of detecting CO emission lines is higher in TDGs (Braine et al. 2001), which could overcome the spatial resolution issue. Moreover, since a TDG’s molecular gas is predicted to be formed *in situ* (Braine

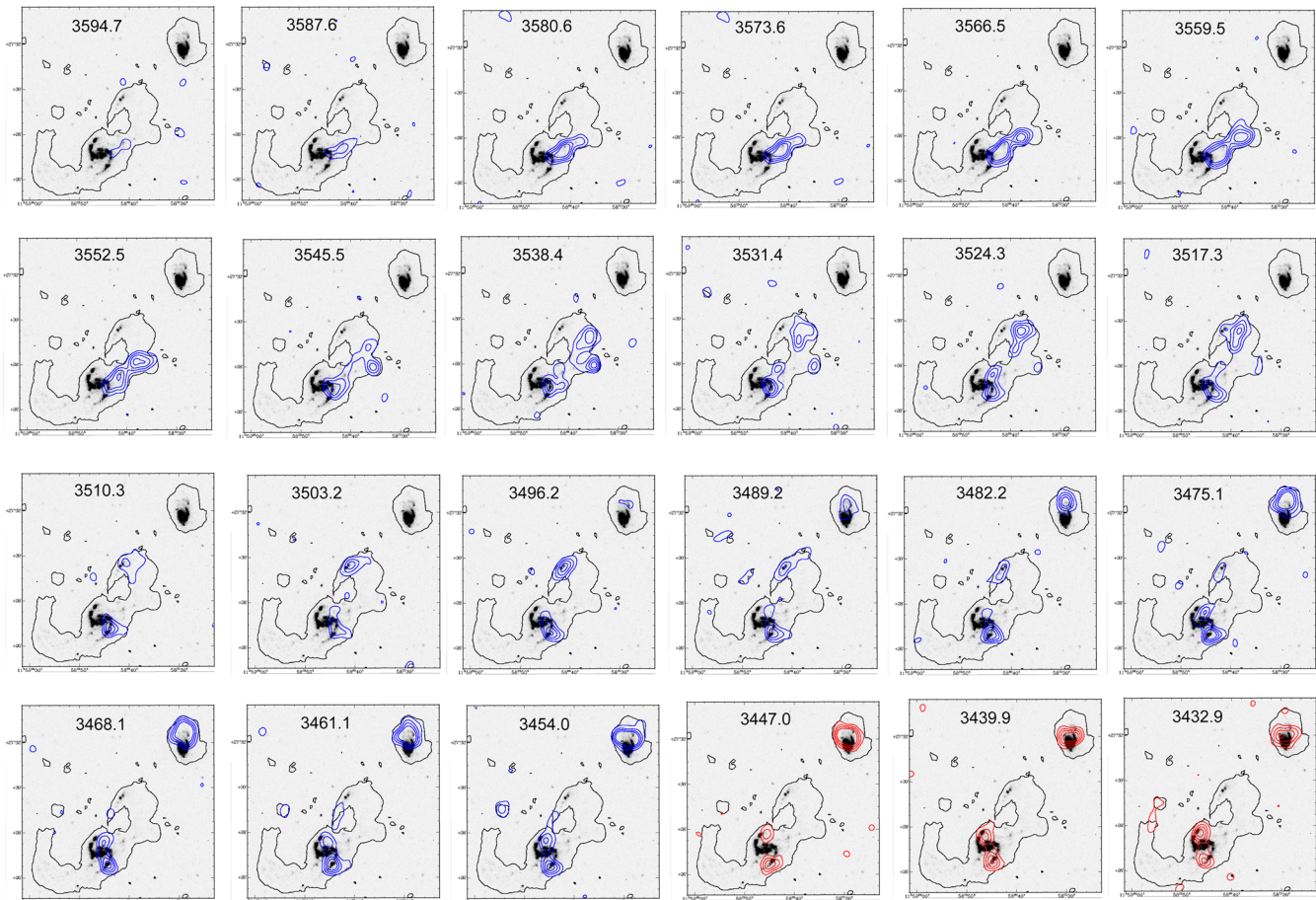


**Figure 8.** Arp 305 H I channel maps from the low-resolution cube – part A. Each channel’s velocity in  $\text{km s}^{-1}$  is shown at the top of each panel with the channel separation  $\sim 7 \text{ km s}^{-1}$ . The contours indicate H I emission, blue contours for H I emission in channels with velocities higher than the pair’s mean optical heliocentric velocity of  $3445 \text{ km s}^{-1}$ . The H I contour colour changes from blue to red at  $3445 \text{ km s}^{-1}$  for channels with velocities below this value. The contour levels are  $1.2 \text{ mJy} \times (3, 5, 7, 9)$ . The black contours are the lowest contours from the low-resolution H I velocity integrated map shown in Fig. 2. A continuation of the channel maps is presented in Fig. 9.

et al. 2001), the molecular gas disc is expected to be more localized to the TDG than H I.

An old stellar component in the Arp 305 tidal bridge is predicted by the Hancock et al. (2009) modelling of the pair interaction. Like the tidal bridges in Smith et al. (2007), the bridge TDG is detected in both the *Spitzer* 3.6 and 4.5  $\mu\text{m}$  band images. In general, it is understood that both bands trace emission from stellar populations with ages  $> 1 \text{ Gyr}$ . However, it is known that both of these bands can be contaminated by emission from strong SF regions, by up to 50 per cent from intermediate-age stars (red supergiant and asymptotic giant branch) and 22 per cent from dust (Meidt et al. 2012). Additionally, the 4.5  $\mu\text{m}$  band suffers from CO absorption (Meidt et al. 2012). We estimated the *Spitzer* 3.6 and 4.5  $\mu\text{m}$  flux densities at  $94.71$  and  $95.26 \mu\text{J}$ , respectively. The *Spitzer* magnitudes (AB) for these bands are  $15.7 \pm 0.3$  and  $15.9 \pm 0.3$ , respectively, and the [3.6]–[4.5] colour is  $\sim -0.2$  mag. Unfortunately, there are inconsistent interpretations for this colour in the literature. For example, fig. 7 of Smith et al. (2005) indicates that the emission from M0 III stars (red giants) has a colour ( $\sim -0.15$ ), close to  $-0.2$ , while Querejeta et al. (2015) state: ‘The expected colour for an old stellar population of ages  $t \sim 2\text{--}12 \text{ Gyr}$  is  $-0.2 < [3.6]\text{--}[4.5] < 0$ ’. Both Smith and Querejeta agree that this colour is not associated with strong dust emission. Also, the [3.6]–[4.5] colour of old ellipticals is negative (Peletier et al. 2012). We conclude that the bridge TDG

is largely free from dust emission, and it is highly probable that its 3.6 and 4.5  $\mu\text{m}$  emission is principally tracing a stellar population formed before the latest interaction by the pair. If this is the case, it is consistent with the stellar debris seeding the TDG scenario. Optical spectroscopy could provide confirmation of this. The stellar mass based on the *Spitzer* 3.6 and 4.5  $\mu\text{m}$  flux is  $\sim 4.1 \times 10^7 M_{\odot}$ , following Eskew, Zaritsky & Meidt (2012). This is higher than the stellar mass estimate by Hancock et al. (2009) of  $(1\text{--}7) \times 10^6 M_{\odot}$ , but still an order of magnitude lower than the H I mass of the TDG, making it a gas-dominated system.

Accepting the limitations of claims that can be made using the currently available data, we find that the Arp 305 bridge TDG differs from our previous TDG H I detections in Arp 202 and Arp 181 (Sengupta et al. 2013, 2014) in having *Spitzer* 3.6 and 4.5  $\mu\text{m}$  counterparts, indicative of an old stellar component. Additionally, Arp 305 TDG has strong UV emission indicating recent SF. This is consistent with a scenario where the central region of the tidal bridge, containing old stars originating in the principal pair, provided the seed potential for the TDG to grow from infalling gas debris. This scenario is quite different from TDG candidates detected in Arp 181 and Arp 202. In those cases, weak optical emission and the absence of *Spitzer* near-infrared emission (Smith et al. 2007) suggests an insignificant old stellar component in those TDGs and supports a scenario where the TDG primarily forms from gas debris

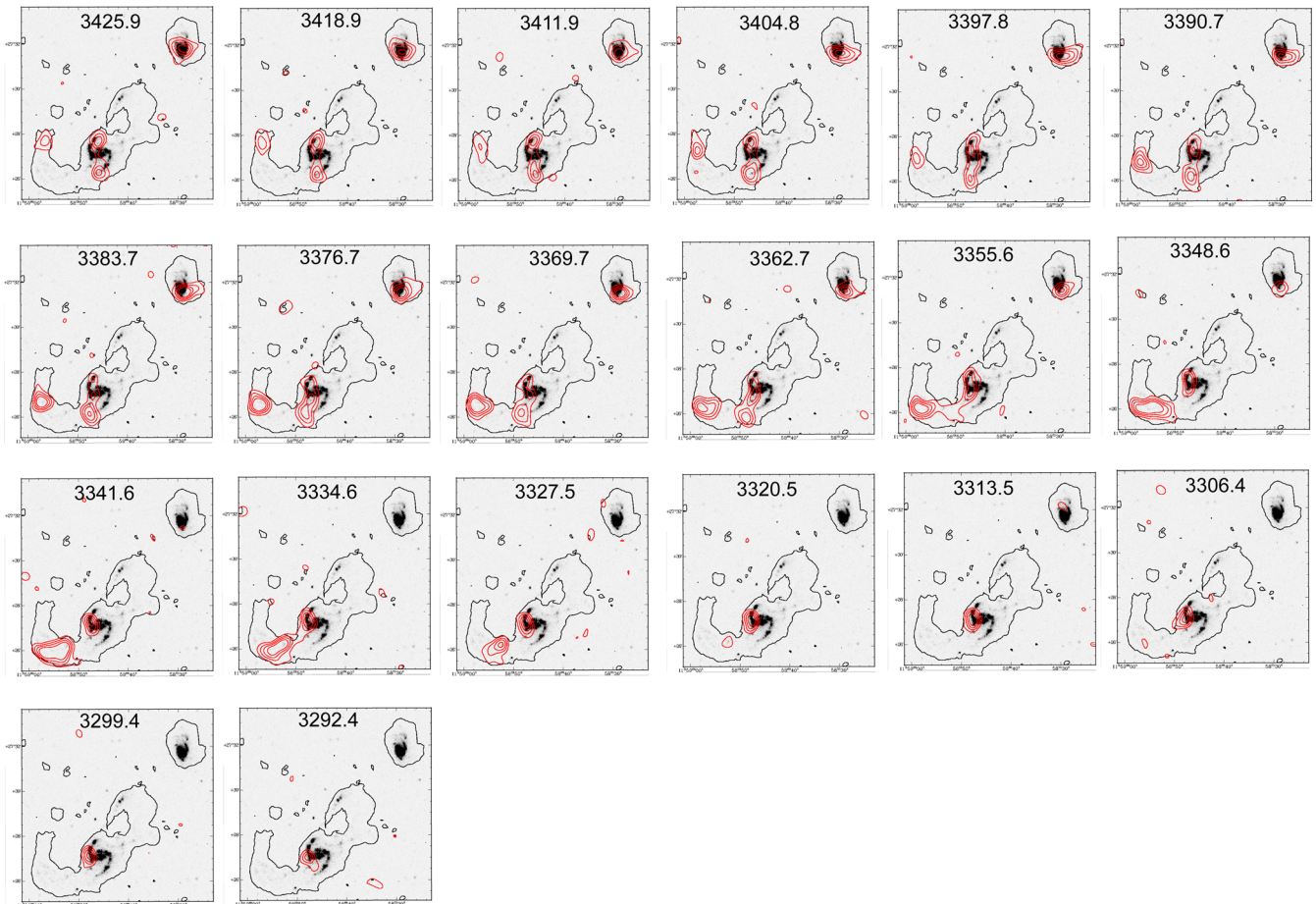


**Figure 9.** Arp 305 H I channel maps from the low-resolution cube – part B. The description of the plot is given in the caption to Fig. 8.

**Table 5.** H I and SF properties of the TDG candidates.

System	TDG candidate	H I column density ( $10^{20}$ atoms $\text{cm}^{-2}$ )	H I map resolution (arcsec)	Estimated time since interaction (Gyr)	Pair $M_*$ ratio	SFR ( $M_\odot \text{ yr}^{-1}$ )	SFE ( $M_\odot \text{ yr}^{-1}/M_\odot$ )
Arp 65	H I maxima	8.3	23	0.2	1:3.0	–	–
Arp 181	TDG	9.9	10	–	1:3.6	–	–
Arp 202	TDG	7.5	23	0.4	1:1.4	0.04	$3.9 \times 10^{-10}$
Arp 305	Bridge TDG	4.1	32	0.4	1:3.3	0.20	$3.0 \times 10^{-10}$

collapse. In Table 5, we compare the H I and SF properties of the TDG candidates and potential TDG host debris we have studied so far. Arp 181’s TDG has no published SFR from any band, and Arp 65’s high column density H I debris does not host a TDG or detected SF activity (Sengupta et al. 2015). Table 5 shows that while the SFR of Arp 305 is about an order of magnitude higher than Arp 202, the star formation efficiency (SFE), defined as SFR per unit H I mass, is similar and is consistent with the low SFE trends of TDGs (Braine et al. 2001). While the comparison of TDGs in Table 5 is inconclusive due to the small sample size, it remains an open question whether the presence of a substantial old stellar population in a TDG significantly affects its SF history and, in particular, the time-scale for TDG formation.

## 5 SUMMARY AND CONCLUDING REMARKS

We have mapped the H I in the Arp 305 interacting pair with the GMRT. Our analysis of the H I morphology and kinematics of the

pair supports the conclusion in Hancock et al. (2009) that the most recent encounter between the pair occurred  $\sim 4 \times 10^8$  yr ago. However, there are H I morphological and kinematic features NW of NGC 4017, not found in models of first encounters for interacting galaxy pairs, which may be remnants of an earlier encounter between the two galaxies. Similar features in M 51-type systems are proposed as debris from earlier encounters. The Arp 305 system shows extended SF in its tidal tails and bridge. The GMRT H I maps lack the spatial resolution for detailed studies of the correlation between individual SF zones and H I column densities, although the extragalactic SF zones in the Arp 305 system are projected at locations with a range of H I column densities with no specific bias towards higher column densities.

The H I morphology and kinematic properties of the bridge TDG candidate include  $M_{\text{H I}} \sim 6.6 \times 10^8 M_\odot$  and  $V_{\text{H I}} = 3500 \pm 7 \text{ km s}^{-1}$  (in good agreement with the velocities of the parent galaxies). Additionally, the linewidth of  $30 \text{ km s}^{-1}$ , modest velocity gradient and SFR of  $0.20 M_\odot \text{ yr}^{-1}$  add to the evidence favouring the bridge

TDG candidate being a genuine TDG. A *Spitzer* 3.6 and 4.5  $\mu\text{m}$  counterpart with a [3.6]–[4.5] colour  $\sim -0.2$  mag suggests a formation scenario containing a substantial old stellar population. Future spectroscopic observations for this TDG are planned to confirm this formation scenario and provide the metallicity of the TDG. Originating from processed material, TDGs are expected to show higher metallicity compared to normal dwarf galaxies, making it a key criterion for the validation for TDG candidates.

## ACKNOWLEDGEMENTS

We thank the staff of the GMRT, who have made these observations possible. The GMRT is operated by the National Centre for Radio Astrophysics of the Tata Institute of Fundamental Research. Support for this work was also provided by the Science Fellowship of POSCO TJ Park Foundation. This work was supported by Fundação para a Ciência e a Tecnologia (FCT) through national funds (UID/FIS/04434/2013) and by FEDER through COMPETE2020 (POCI-01-0145-FEDER-007672). TS acknowledges the support by the fellowship SFRH/BPD/103385/2014 funded by FCT (Portugal) and POPH/FSE (EC). This research has made use of the NASA/IPAC Extragalactic Database (NED), which is operated by the Jet Propulsion Laboratory, California Institute of Technology, under contract with the National Aeronautics and Space Administration. This research has made use of the Sloan Digital Sky Survey (SDSS). Funding for the SDSS and SDSS-II has been provided by the Alfred P. Sloan Foundation, the Participating Institutions, the National Science Foundation, the U.S. Department of Energy, the National Aeronautics and Space Administration, the Japanese Monbukagakusho, the Max Planck Society and the Higher Education Funding Council for England. The SDSS website is <http://www.sdss.org/>. This research made use of APLPY, an open-source plotting package for PYTHON, hosted at <http://aplp.github.com>.

## REFERENCES

- Baars J. W. M., Genzel R., Pauliny-Toth I. I. K., Witzel A., 1977, *A&A*, 61, 99
- Barnes J. E., 1992, *ApJ*, 393, 484
- Begum A., Chengalur J. N., Karachentsev I. D., Kaisin S. S., Sharina M. E., 2006, *MNRAS*, 365, 1220
- Bell E. F., McIntosh D. H., Katz N., Weinberg M. D., 2003, *ApJS*, 149, 289
- Blanton M. R., Hogg D. W., Bahcall N. A., Brinkmann J., Britton M., Connolly A. J., Csabai I., Fukugita M., 2003, *ApJ*, 592, 819
- Boselli A., Boissier S., Cortese L., Buat V., Hughes T. M., Gavazzi G., 2009, *ApJ*, 706, 1527
- Braine J., Duc P.-A., Lisenfeld U., Charmandaris V., Valjejo O., Leon S., Brinks E., 2001, *A&A*, 378, 51
- de Mello D. F., Urrutia-Viscarra F., Mendes de Oliveira C., Torres-Flores S., Carrasco E. R., Cypriano E., 2012, *MNRAS*, 426, 2441
- Duc P.-A., Mirabel I. F., 1999, in Barnes J. E., Sanders D. B., eds, *Proc. IAU Symp. 186, Galaxy Interactions at Low and High Redshift*. Kluwer, Dordrecht, p. 61
- Duc P.-A., Brinks E., Wink J. E., Mirabel I. F., 1997, *A&A*, 326, 537
- Duc P.-A., Brinks E., Springel V., Pichardo B., Weilbacher P., Mirabel I. F., 2000, *AJ*, 120, 1238
- Duc P.-A., Bournaud F., Masset F., 2004, *A&A*, 427, 803
- Eskew M., Zaritsky D., Meidt S., 2012, *AJ*, 143, 139
- Flores H., Hammer F., Fouquet S., Puech M., Kroupa P., Yang Y., Pawlowski M., 2016, *MNRAS*, 457, L14
- Hancock M., Smith B. J., Struck C., Giroux M. L., Hurlock S., 2009, *AJ*, 137, 4643
- Haynes M. P., Giovanelli R., 1984, *AJ*, 89, 758
- Haynes M. P. et al., 2011, *AJ*, 142, 170
- Hibbard J. E., Bianchi L., Thilker D. A., Rich R. M., Schiminovich D., Xu C. K., Neff S. G., 2005, *ApJL*, 619, L87
- Holwerda B. W., Pirzkal N., Cox T. J., de Blok W. J. G., Weniger J., Bouchard A., Blyth S.-L., van der Heyden K. J., 2011, *MNRAS*, 416, 2426
- Howard S., Byrd G. G., 1990, 99, 1798
- Huchtmeier W. K., Richter O.-G., 1989, *A General Catalog of HI Observations of Galaxies*. The Reference Catalog. Springer-Verlag, Berlin Heidelberg, p. 350
- Kennicutt R. C., Jr, 1989, *ApJ*, 344, 685
- Lelli F. et al., 2015, *A&A*, 584, 113
- Lewis B. M., Helou G., Salpeter E. E., 1985, *ApJS*, 59, 161
- Makarov D., Prugniel P., Terekhova N., Courtois H., Vauglin I., 2014, *A&A*, 570, A13
- Maybath A., Masiero J., Hibbard J. E., Charlton J. C., Palma C., Knierman K. A., English J., 2007, *MNRAS*, 381, 59
- Meidt S. E., Schinnerer E., Knapen J. H., Bosma A., Athanassoula E., Sheth K., 2012, *ApJ*, 744, 17
- Mullan B. et al., 2013, *ApJ*, 768, 194
- Neff S. G., Thilker D. A., Seibert M., Gil de Paz A., Bianchi L., Schiminovich D., Martin D. C., 2005, *ApJ*, 619, L91
- Nikiel-Wroczyński B., Soida M., Bomans D. J., Urbanik M., 2014, *ApJ*, 786, 144
- Oh S. H., Kim W.-T., Lee H. M., Kim J., 2008, *ApJ*, 683, 94
- Peletier R. F., Kutdemir E., van der Wolk G., Falcón-Barroso J., Bacon R., Bureau M., Cappellari M., 2012, *MNRAS*, 419, 2031
- Planck Collaboration I, 2014, *A&A*, 571, A1
- Querejeta M. et al., 2015, *ApJS*, 219, 5
- Ramella M., Geller M. J., Pisani A., da Costa L. N., 2002, *AJ*, 123, 2976
- Salo H., Laurikainen E., 1993, *ApJ*, 410, 586
- Schechtman-Rook A., Hess K. M., 2012, *ApJ*, 750, 171
- Sengupta C., Dwarakanath K. S., Saikia D. J., Scott T. C., 2013, *MNRAS*, 431, L1
- Sengupta C., Scott T. C., Dwarakanath K. S., Saikia D. J., Sohn B. W., 2014, *MNRAS*, 444, 558
- Sengupta C., Scott T. C., Paudel S., Saikia D. J., Dwarakanath K. S., Sohn B. W., 2015, *A&A*, 584, A114
- Skillman E. D., Terlevich R., Teuben P. J., van Woerden H., 1988, *A&A*, 198, 33
- Smith B. J., Struck C., Appleton P. N., Charmandaris V., Reach W., Eitter J. J., 2005, 130, 2117
- Smith B. J., Struck C., Hancock M., Appleton P. N., Charmandaris V., Reach W. T., 2007, *AJ*, 133, 791
- Smith B. J., Giroux M. L., Struck C., Hancock M., 2010, *AJ*, 139, 1212
- Theureau G., Hanski M. O., Coudreau N., Hallet N., Martin J.-M., 2007, *A&A*, 465, 71
- Torres-Flores S., Epinat B., Amram P., Plana H., Mendes de Oliveira C., 2011, *MNRAS*, 416, 1936
- Torres-Flores S., de Oliveira C. M., de Mello D. F., Scarano S., Urrutia-Viscarra F., 2012, *MNRAS*, 421, 3612
- van Moorsel G. A., 1983, 54, 19

This paper has been typeset from a  $\text{\TeX}/\text{\LaTeX}$  file prepared by the author.